Official journal of the CIOMP 2047-7538
www.nature.com/lsa

ARTICLE Open Access

Rational strategy for power doubling of monolithic multijunction III-V photovoltaics by accommodating attachable scattering waveguides

Shin Hyung Lee[1], Hyo Jin Kim[2], Jae-Hyun Kim[3], Gwang Yeol Park[2], Sun-Kyung Kim[3] and Sung-Min Lee[4,5]✉

Abstract

While waveguide-based light concentrators offer significant advantages, their application has not been considered an interesting option for assisting multijunction or other two-terminal tandem solar cells. In this study, we present a simple yet effective approach to enhancing the output power of transfer-printed multijunction InGaP/GaAs solar cells. By utilizing a simply combinable waveguide concentrator featuring a coplanar waveguide with $BaSO_4$ Mie scattering elements, we enable the simultaneous absorption of directly illuminated solar flux and indirectly waveguided flux. The deployment of cells is optimized for front-surface photon collection in monofacial cells. Through systematic comparisons across various waveguide parameters, supported by both experimental and theoretical quantifications, we demonstrate a remarkable improvement in the maximum output power of a 26%-efficient cell, achieving an enhancement of ~93% with the integration of the optimal scattering waveguide. Additionally, a series of supplementary tests are conducted to explore the effective waveguide size, validate enhancements in arrayed cell module performance, and assess the drawbacks associated with rear illumination. These findings provide a comprehensive understanding of our proposed approach towards advancing multi-junction photovoltaics.

Introduction

Monolithic multijunction III-V compound semiconductor solar cells are widely recognized as ultrahigh-performance photovoltaics, stemming from their favorable material properties such as direct bandgap, high carrier mobility, low-temperature coefficient, and superior radiative hardness[1–5]. These types of solar cells are simply configured into two-terminal photovoltaics without an increase in parasitic absorption loss, which is a practically attractive feature as the complexity of photovoltaic module implementation can be reduced[6,7]. Despite such compelling features, their high manufacturing cost has been a hurdle for the broad application in terrestrial photovoltaics[8]. One direct approach for improving their cost-effectiveness might be reducing materials consumption. This case can be achieved by designing minimal epitaxial stacks (e.g., lattice-matched structures) or reusing growth wafers (e.g., epitaxial lift-off process)[9–11]. Alternatively, an indirect approach to addressing this issue involves improving cell utilization by increasing power generation capability with light concentrators[12–14]. A concentrator intensifies the solar photon flux incident to solar cells, thus enabling solar cells to generate the boosted output power beyond a value available under unconcentrated illumination. However, the typical light concentrators comprising optics components are not actually cost-effective because of the sophisticated module assembly level and the essential maintenance system. Moreover, they do not operate properly under diffuse sunlight, impeding their effectiveness in reducing the levelized cost of electricity.

In contrast, waveguide-based light concentrators do not diminish the cost-reduction benefits due to simple module construction. The waveguide concentrator consists of a transparent multimode slab waveguide containing luminescent, scattering, or both elements capable of redirecting photon propagation[15–22]. By diverting

Correspondence: Sung-Min Lee (sungminlee@hanyang.ac.kr)
[1]School of Electrical Engineering, Korea Advanced Institute of Science and Technology (KAIST), Daejeon 34141, Republic of Korea
[2]Optoelectronic Convergence Research Center, Korea Photonics Technology Institute, Gwangju 61007, Republic of Korea
Full list of author information is available at the end of the article
These authors contributed equally: Shin Hyung Lee, Hyo Jin Kim.

photons towards solar cells embedded within the waveguide or mounted at the waveguide edges through total internal reflection, photon concentration becomes possible without the need for precise module construction. Its effective operation under diffusely incident sunlight is another notable advantage of the waveguide concentrator. Despite these advantages, the waveguide concentrator has not been considered a promising option for reinforcing multijunction or other two-terminal tandem solar cells[6,23,24]. This is due to several concerns regarding performance synergy. While the multijunction cells, typically designed as monofacial cells, require front-side photon incidence to achieve a balanced output current from series-connected subcells, the bifacial cell is an effective configuration to capture photons traveling within the waveguide. Additionally, as multijunction cells are designed to operate efficiently across the entire solar spectrum, the waveguide concentrator with spectral elements responding to a narrow photon spectrum (e.g., luminophores) may not be effective with them. Rigorous tuning of spectral elements in the waveguide concentrator can alleviate the ineffectiveness of their finite spectrum responses[6]; however, the level of output power amplification still remains limited, thus necessitating the development of more advanced waveguide concentrator technology compatible with high photovoltaic-capable multijunction cells.

In this regard, the present study introduces a straightforward yet effective approach to amplifying the output power of multijunction III-V solar cells by employing a simply combinable waveguide concentrator. Microscale InGaP/GaAs double-junction solar cells are arranged within a transparent slab medium through the transfer-printing assembly method, where the cell deployment is optimized to enhance front-surface photon collection, both for directly incident solar flux and waveguided solar flux. To enable broad-spectrum solar photons to be waveguided[20–22], we separately prepare a photon scattering medium of a sticky elastomer slab with $BaSO_4$ particles and attach it underneath the cell-incorporated transparent waveguide slab. The key features of the present approach are (i) the optimal integration design of multijunction cells with waveguides to concentrate broadband photon flux preferentially on the front cell surfaces and (ii) the simplicity of module implementation that allows considerable augmentation of the multijunction cell output power without the need for complicated process addition. Based on experimental characterization and numerical modeling, systematic investigations to access photon waveguide and collection properties at various waveguide parameters and scattering element conditions are conducted to find the maximum benefits of waveguide concentrators with multijunction III-V solar cells.

Results

Module design and fabrication

Figure 1a schematically depicts the proposed module design and its fabrication steps. The module comprises two-terminal microscale InGaP/GaAs solar cells (area; $A_c = 500 \times 500\ \mu m^2$) and upper (polyurethane; PU), lower (glass), and scattering (polydimethylsiloxane; PDMS) waveguide sublayers. The solar cells are positioned horizontally between the upper and lower waveguide sublayers. The scattering waveguide sublayer contains disorderly distributed $BaSO_4$ particles, and an Ag backside reflector (BSR) is placed at the bottom surface of this waveguide. This module configuration allows two distinct routes for the incident solar photons to reach the solar cells. One route involves the direct photon incidence facilitated by the coplanar cell-to-waveguide arrangement. The other route follows an indirect path, in which the solar photons incident to the outside of the cells are redirected through collisions with the $BaSO_4$ particles in the scattering waveguide sublayer, ultimately moving toward the embedded solar cells. This indirect route is well compatible with multijunction cell features: (i) A waveguide channel of the upper sublayer facilitates photon collection at the front cell surface. (ii) The scattering response across the broad spectral range empowers balanced photocurrent enhancements for the top and bottom subcells.

The module was created through straightforward fabrication processes. Initially, a package of releasable InGaP/GaAs solar cells was formed on a growth wafer, involving sequent steps such as contact metallization, antireflection coating (ARC, 60 nm ZnS), cell isolation, and undercut etching. Subsequently, a specific InGaP/GaAs cell was transfer-printed onto a glass substrate serving as a transparent lower waveguide sublayer (thickness; $t_{lw} = 700\ \mu m$) using a relief-patterned PDMS stamp. Following the formation of interconnection electrodes and the addition of a transparent upper waveguide sublayer (PU, $t_{uw} = 420\ \mu m$), a fully operational module with the InGaP/GaAs solar cell was ready. At this stage, the module, before incorporating the scattering waveguide sublayer, demonstrated a power conversion efficiency (PCE) of ~26.2% with a short-circuit current density (J_{sc}) of ~13.8 mA cm^{-2}, an open-circuit voltage (V_{oc}) of ~2.24 V, and a fill-factor (FF) of ~84.7%. Detailed information on epitaxial stacks on the growth wafer and fabrication procedures can be found in the Methods section and Figs. S1 and S2. A scattering waveguide sublayer ($t_{sw} = 1900\ \mu m$) was separately prepared by thermal curing of PDMS mixed with dispersed $BaSO_4$ particles, where a fraction of $BaSO_4$/PDMS in weight (f_{BaSO4}) ranged from 0.05 to 15.4 wt%. An Ag BSR ($t = 100$ nm) was deposited afterward. Since this cured $BaSO_4$-PDMS exhibited a self-adhesive property and hence easily adhered to a flat surface[25,26], the final step for combining the scattering sublayer with the module was completed through a simple

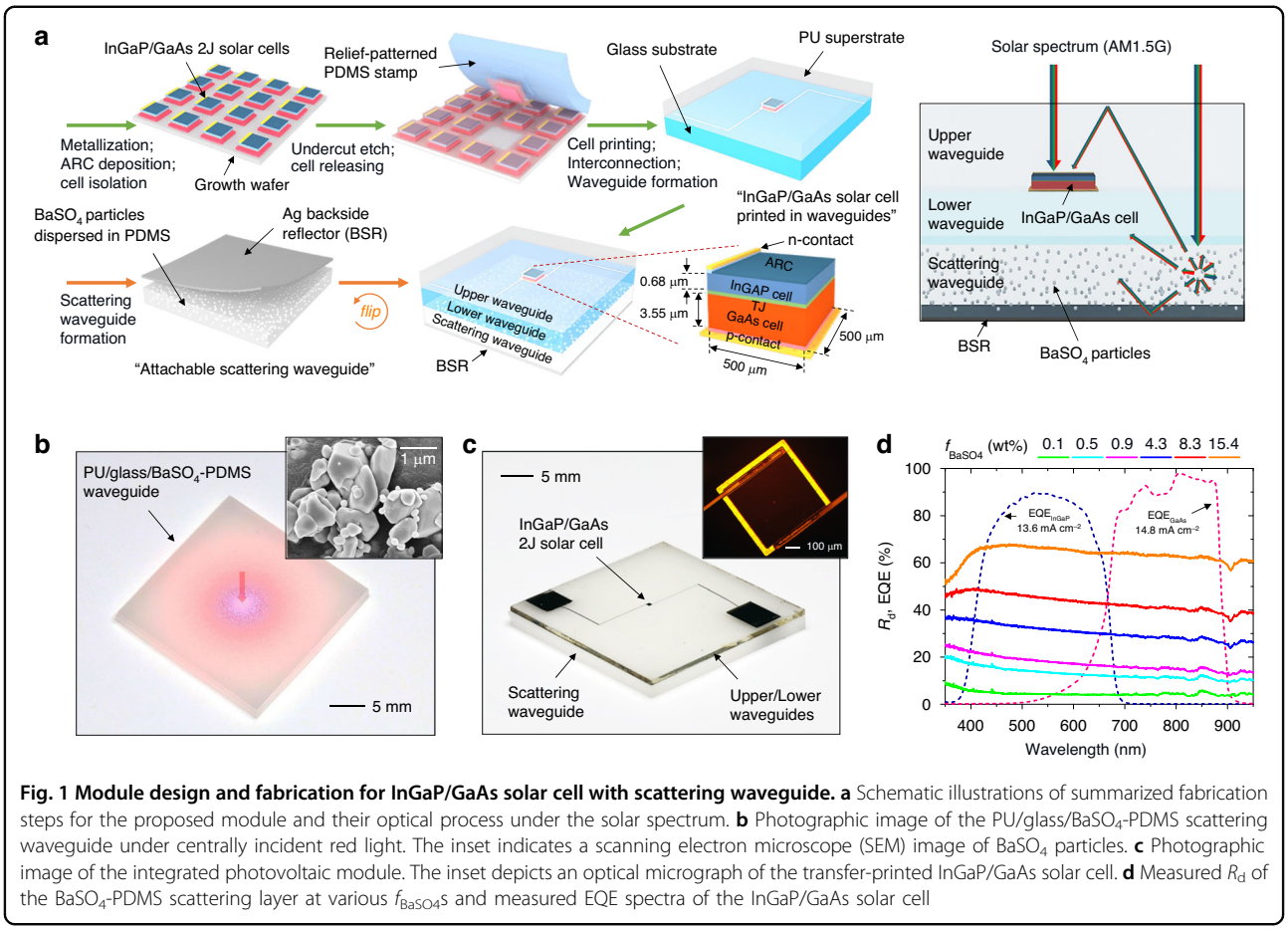

Fig. 1 Module design and fabrication for InGaP/GaAs solar cell with scattering waveguide. a Schematic illustrations of summarized fabrication steps for the proposed module and their optical process under the solar spectrum. **b** Photographic image of the PU/glass/$BaSO_4$-PDMS scattering waveguide under centrally incident red light. The inset indicates a scanning electron microscope (SEM) image of $BaSO_4$ particles. **c** Photographic image of the integrated photovoltaic module. The inset depicts an optical micrograph of the transfer-printed InGaP/GaAs solar cell. **d** Measured R_d of the $BaSO_4$-PDMS scattering layer at various f_{BaSO4}s and measured EQE spectra of the InGaP/GaAs solar cell

physical attachment process. A photographic image of the assembled upper/lower/scattering waveguide is presented in Fig. 1b, allowing for the observation of the spreading behavior of centrally incident photons within this waveguide. A complete InGaP/GaAs cell module integrated with the suggested waveguide combination is shown in Fig. 1c.

Balanced subcell photocurrents are crucial for enhancing the overall output current of InGaP/GaAs cells, given the series-connected subcell configuration. As depicted in the external quantum efficiency (EQE) response in Fig. 1d, the experimental sample without scattering elements, which represents the case of only direct photon incidence, exhibited reasonably balanced yet slightly discrepant photocurrent densities (J_{ph}s) between the top and bottom subcells ($J_{ph,top} = 13.6\ mA\ cm^{-2} < J_{ph,bot} = 14.8\ mA\ cm^{-2}$) under the non-concentrated AM1.5 G solar illumination. Therefore, photon flux indirectly supplied to the InGaP/GaAs cell from the waveguide needs to boost both subcell photocurrents, with a slight bias toward the current-limiting subcell (i.e., the top subcell) for optimal balance. The $BaSO_4$ particles (size = 200 ~ 700 nm) dispersed in the PDMS waveguide exhibited the white scattering behavior that covered the entire absorption spectra of the top and bottom subcells (Figs. S3 and S4). This implies that scattered photons in the waveguide can influence both subcell photocurrents. Meanwhile, the overall diffuse reflectance (R_d) of the $BaSO_4$-PDMS scattering waveguide monotonically increased with an increase in the f_{BaSO4} due to raised photon collision events (Fig. 1d). Notably, R_d was moderately higher at shorter wavelengths, suggesting that scattered photons can contribute more effectively to the top subcell. The inclusion of an Ag BSR further amplified the R_d of the $BaSO_4$-PDMS, indicating that stronger scattering can be anticipated at a given f_{BaSO4} (Fig. S5).

Waveguide parameter optimization

The photon delivery property of the waveguide concentrator depends on several factors, including the geometric and optical parameters of the upper, lower, and scattering waveguide sublayers. These parameters affect the quantity and distribution of photons trapped and guided within the waveguide, ultimately regulating the amount of collected photons at the front surface of the InGaP/GaAs cell embedded within. To gain insights into the effects of these parameters and identify their optimal values for maximizing

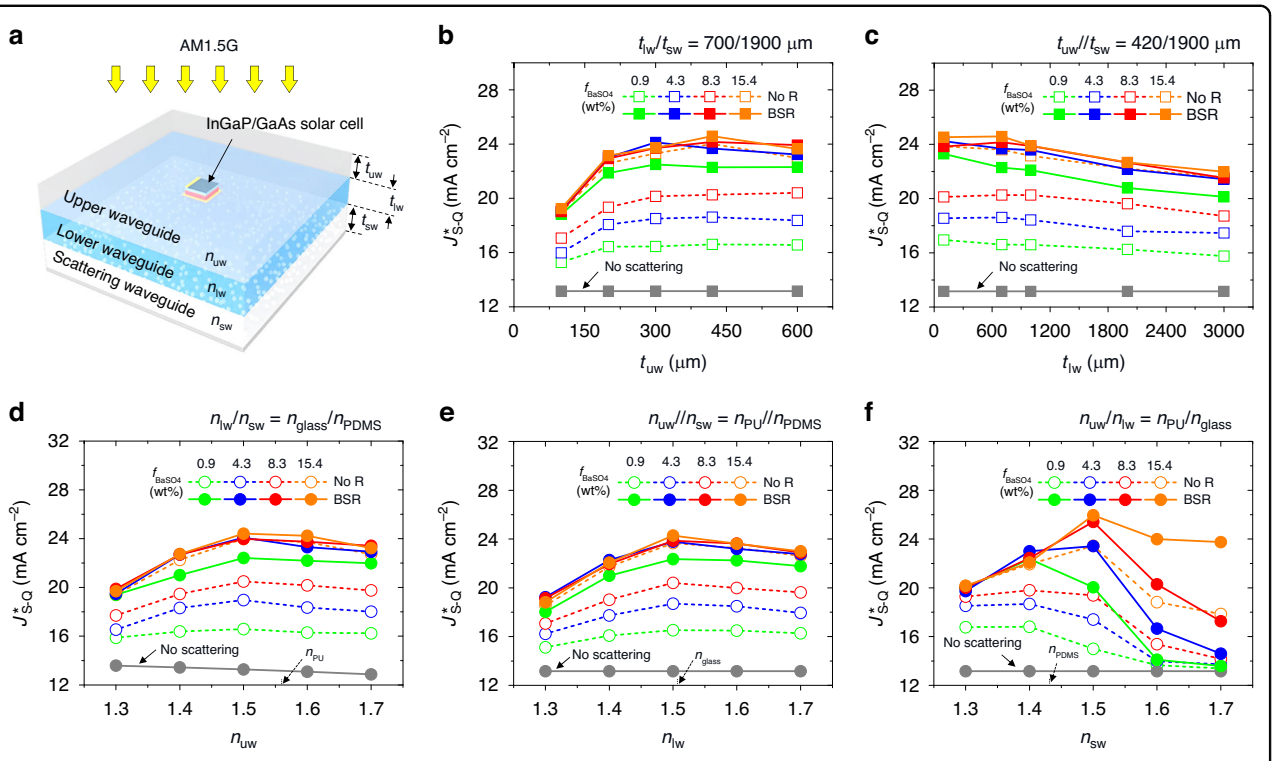

Fig. 2 Numerical calculations for waveguide parameter optimization. a Schematic illustrations of the simulated module configuration. Calculated J^*_{S-Q}s for PU/glass/$BaSO_4$-PDMS ($n_{PU}/n_{glass}/n_{PDMS} \approx 1.56/1.51/1.43$) waveguide modules at various t_{uw}s under fixed $t_{lw}/t_{sw} = 700/1900$ μm (**b**) and at various t_{lw}s under fixed $t_{uw}//t_{sw} = 420//1900$ μm (**c**). Calculated J^*_{S-Q}s for PU/glass/$BaSO_4$-PDMS ($t_{uw}/t_{lw}/t_{sw} = 420/700/1900$ μm) waveguide modules if n_{uw} (**d**), n_{lw} (**e**), and n_{sw} (**f**) change

cell performance, we conducted optical modeling for the experimental module (as depicted in Fig. 2a) with various thicknesses (t_{uw}, t_{lw}, t_{sw}) and refractive indices (n_{uw}, n_{lw}, n_{sw}) of the upper, lower, and scattering waveguide sublayers. Using the 3-dimensional ray-tracing simulation, an amount of collected photon flux at the front cell surface was calculated, where details of the simulation setup and representative ray-tracing results can be found in Table. S1 and Fig. S6. Assuming that the collected photon flux obtained in the ray-tracing simulation was normally incident to an InGaP/GaAs cell, the photon absorption in the emitter and base layers, which are primarily responsible for photocurrent generation[6,27], was assessed using the multilayer transfer-matrix formula[28,29]. A quantitative comparison of the cell performance was enabled by evaluating the Shockley-Queisser current limit (denoted as J^*_{S-Q}) based on the detailed balance analyses given by the equation below[30–34].

$$J^*_{S-Q} = q\int_0^\infty A_{e/b}(E)\Phi_S(E)dE \quad (1)$$

Here, a superscript '*' indicates the cell area (A_c) normalization. q, $A_{e/b}$, Φ_s, E are the electron charge, the emitter/base absorptance, the collected solar flux at the front cell surface, and the photon energy, respectively. The output J^*_{S-Q} of the InGaP/GaAs cell was determined by choosing a smaller J^*_{S-Q} value against the InGaP and GaAs subcells, considering the current matching rule of series-connected two-terminal multijunction configuration[33].

Figure 2b, c present the calculated J^*_{S-Q}s for the experimental upper/lower/scattering configuration of PU/glass/$BaSO_4$-PDMS ($n_{PU}/n_{glass}/n_{PDMS} \approx 1.56/1.51/1.43$) when changing t_{uw} and t_{lw} values at different f_{BaSO4} levels of the $BaSO_4$-PDMS. Under fixed t_{lw} and t_{sw} (700 and 1900 μm), the J^*_{S-Q} exhibited a specific trend when t_{uw} was increased from 100 to 600 μm (Fig. 2b). Initially, there was an increase in J^*_{S-Q}, followed by a saturation effect. This trend indicates that photon guidance to the front cell surface is facilitated by the appropriately thick upper sublayer serving the above-cell waveguide channel in the coplanar-type arrangement. Simultaneously, a higher f_{BaSO4} in the scattering sublayer resulted in a larger J^*_{S-Q}, regardless of t_{uw}. This effect was due to more photons being scattered, contributing to the waveguiding process. The impact of increasing f_{BaSO4} on J^*_{S-Q} varied depending on whether a BSR was included or not. With increasing f_{BaSO4}, the module without the BSR (referred to as the

BSR-less module) presented a gradual $J^*_{S\text{-}Q}$ improvement; by contrast, the module with the BSR (referred to as the BSR-added module) showed a rapid increase in $J^*_{S\text{-}Q}$ followed by saturation. This behavior can be explained by the augmented photon scattering in the BSR-added module, similar to the intensified scattering effect observed in the high-f_{BaSO4} case. Note that if t_{uw} exceeded a certain threshold (approximately over 400 μm), the $J^*_{S\text{-}Q}$ tended to decrease for modules with strong photon scattering (e.g., the BSR-less modules with $f_{BaSO4} \geq 15.4$ wt %, the BSR-added modules with $f_{BaSO4} \geq 4.3$ wt%) due to increased propagation loss. Further details on propagation loss will be discussed later. Meanwhile, increasing t_{lw} while keeping t_{uw} and t_{sw} constant (420 and 1900 μm) had a negative effect on $J^*_{S\text{-}Q}$ for all module cases (Fig. 2c). This is because the lower waveguide sublayer served as a pathway for photons that were not captured at the front cell surface. However, modules with f_{BaSO4} values exceeding 8.3 wt% showed relatively stable $J^*_{S\text{-}Q}$ until t_{lw} reached ~700 μm. This stability was attributed to less contribution of long-distance traveling photons to $J^*_{S\text{-}Q}$, which provided a design margin for t_{lw}.

The $J^*_{S\text{-}Q}$ variations with changes in sublayer refractive indices are provided in Fig. 2d–f. In these calculations, one sublayer of the experimental PU/glass/$BaSO_4$-PDMS waveguide ($t_{uw}/t_{lw}/t_{sw} = 420/700/1900$ μm) was replaced by a non-extinction material with a refractive index ranging from 1.3 to 1.7, while constraining other sublayer materials consistent. Figure 2d depicts the case of changing n_{uw} at fixed n_{lw}/n_{sw} of n_{glass}/n_{PDMS} (≈ 1.51/1.43). Regardless of f_{BaSO4} and BSR conditions, all modules showed their highest $J^*_{S\text{-}Q}$ values at n_{uw} around n_{lw}, because suppressed reflection at an interface of the upper/lower sublayers facilitated the photon quantity at the above-cell waveguide channel. In contrast to the slight $J^*_{S\text{-}Q}$ reduction for the case of $n_{uw} > n_{lw}$, the $J^*_{S\text{-}Q}$ reduction for the opposite case was significant. This accelerated $J^*_{S\text{-}Q}$ reduction can be understood as follows: when n_{uw} was below n_{sw} (a material where momentum change occurs), a condition for total internal reflection could be satisfied, meaning that scattered photons with high in-plane momentum did not enter the upper sublayer. In Fig. 2e, if fixing $n_{uw}//n_{sw}$ to $n_{PU}//n_{PDMS}$ (≈ 1.56//1.43), the maximum $J^*_{S\text{-}Q}$ for all modules appeared at n_{lw} around 1.5, which is in the middle of n_{uw} and n_{sw}. This result is expected, as this n_{lw} condition matched the minimum reflection loss for scattered photons toward the above-waveguide channel, considering both the reflection boundaries between scattering/lower sublayers and lower/upper sublayers. At $n_{lw} < n_{sw}$, a critically low $J^*_{S\text{-}Q}$ was observed due to total internal reflection, similar to the case of $n_{uw} < n_{sw}$ in Fig. 2d. Meantime, a case of changing n_{sw} under fixed n_{uw}/n_{lw} ($n_{PU}/n_{glass} \approx 1.56/1.51$) in Fig. 2f exhibited $J^*_{S\text{-}Q}$ variation behavior corresponding to the cases of changing n_{uw} or n_{lw}. The best $J^*_{S\text{-}Q}$ tended to exist at n_{sw} around n_{lw} due to minimal reflection loss, while the worst $J^*_{S\text{-}Q}$ emerged at $n_{sw} > n_{lw}$ due to total internal reflection generation. However, at the condition of $n_{sw} < n_{lw}$ (also $n_{sw} < n_{uw}$), which was suboptimal for reflection loss, the highest $J^*_{S\text{-}Q}$ was unexpectedly observed for modules with less photon scattering (e.g., the BSR-less modules with $f_{BaSO4} \leq 8.3$ wt%, the BSR-added modules with $f_{BaSO4} \leq 0.9$ wt%). This $J^*_{S\text{-}Q}$ variation behavior was because the weak scattering sublayer provided a comparatively active propagation path acting as a photon loss channel, and decreasing n_{sw} alleviated the propagating photon density in this loss channel.

Photovoltaic performance

Figure 3a, b shows representative density-voltage (J^*-V) curves of experiment InGaP/GaAs modules without and with BSR, respectively, at various f_{BaSO4} levels under the stimulated AM 1.5 G solar spectrum (100 mW cm^{-2}). Derived photovoltaic parameters of these modules are

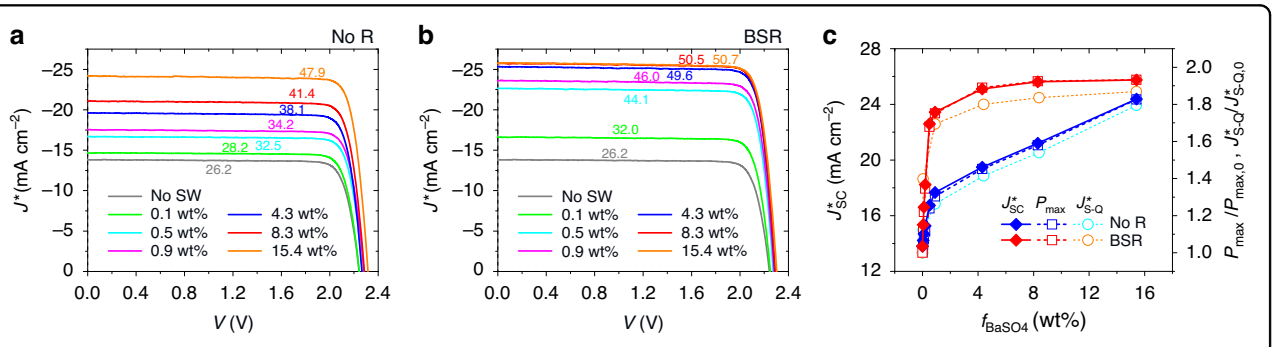

Fig. 3 Photovoltaic performance of InGaP/GaAs solar cell with scattering waveguide. Representative J^*-V curves of the BSR-less (**a**) and BSR-added (**b**) modules measured under the AM 1.5 G solar spectrum (100 mW cm^{-2}) at various f_{BaSO4}s. The term 'no SW' means the control module without $BaSO_4$ particles. **c** Measured J^* and $P_{max}/P_{max,0}$ and calculated $J^*_{S\text{-}Q}/J^*_{S\text{-}Q,0}$ for the modules as a function of f_{BaSO4}. $P_{max,0}$ and $J^*_{S\text{-}Q,0}$ indicate P_{max} and $J^*_{S\text{-}Q}$ of the control module, respectively

Table 1 Photovoltaic characteristics of various conditions for InGaP/GaAs solar cell under the AM 1.5 G illumination (100 mW cm^{-2})

f_{BaSO4} (wt%)	J^*_{sc} (mA cm^{-2})		V_{oc} (V)		FF (%)		P_{max}/A_c (mW cm^{-2})[a]	
	No R	BSR	No R	BSR	No R	BSR	No R	BSR
0 (control)	13.80 ± 0.04[b]		2.24 ± 0.02		84.7 ± 0.7		26.23 ± 0.30	
0.1	14.68 ± 0.03	16.61 ± 0.01	2.24 ± 0.01	2.25 ± 0.01	85.5 ± 0.2	85.5 ± 0.2	28.18 ± 0.07	32.01 ± 0.08
0.5	16.74 ± 0.10	22.60 ± 0.07	2.26 ± 0.01	2.27 ± 0.01	85.7 ± 0.2	85.6 ± 0.2	32.50 ± 0.20	44.05 ± 0.05
0.9	17.66 ± 0.20	23.44 ± 0.25	2.26 ± 0.02	2.29 ± 0.02	85.5 ± 0.5	85.5 ± 0.2	34.20 ± 0.46	45.95 ± 0.50
4.3	19.48 ± 0.29	25.10 ± 0.43	2.28 ± 0.02	2.30 ± 0.03	85.6 ± 0.3	85.6 ± 0.3	38.07 ± 0.40	49.56 ± 0.50
8.3	21.20 ± 0.44	25.62 ± 0.43	2.28 ± 0.02	2.30 ± 0.03	85.6 ± 0.3	85.6 ± 0.2	41.43 ± 0.59	50.48 ± 1.07
15.4	24.38 ± 0.21	25.75 ± 0.21	2.29 ± 0.03	2.30 ± 0.03	85.6 ± 0.2	85.5 ± 0.3	47.90 ± 0.15	50.68 ± 0.37

[a]P_{max}/A_c indicates the maximum output power normalized by a cell area
[b]These are statistical values of average and standard deviation obtained from 10 measurements

provided in Table 1. Compared to the control module without the $BaSO_4$ scattering elements (i.e., PU/glass/PDMS waveguide) ($J^*_{sc} = 13.8$ mA cm^{-2}, $V_{oc} = 2.24$ V, FF = 84.7%, $P_{max}/A_c = 26.2$ mW cm^{-2}), the modules incorporating the $BaSO_4$-PDMS scattering sublayer dramatically increased the J^*_{sc} and slightly enhanced the V_{oc} without degradation of the FF, meaning that boosting power generation by the scattering sublayer was operated well. When examining the case of the BSR-less modules (Fig. 3a), we observe that the J^*_{sc} rose from 13.8 to 17.66 mA cm^{-2} even at a low f_{BaSO4} level, such as $f_{BaSO4} = 0.9$ wt%. The J^*_{sc} nearly linearly increased further as promoting the f_{BaSO4} from 0.9 wt%, resulting in 24.38 mA cm^{-2} and hence $P_{max}/A_c = 47.9$ mW cm^{-2} at $f_{BaSO4} = 15.4$ wt% (82.6% power increase against the control device value). By contrast, in the case of the BSR-added modules (Fig. 3b), the J^*_{sc} augmented rapidly as increasing f_{BaSO4} level initially and became saturated after $f_{BaSO4} \geq 4.3$ wt%. The calculated $J^*_{S\text{-}Q}$s (Fig. S7) values were compared with the measured J^*_{sc}s, as shown in Fig. 3c. The consistent variation with changes in f_{BaSO4} was observed, indicating analyses implemented in the calculation process are valid for the measured results: The photon scattering contribution is enhanced more at higher f_{BaSO4} and adding the BSR. The best module performance can be found in the BSR-added module with $f_{BaSO4} = 15.4$ wt%, which was $J^*_{sc} = 25.75$ mA cm^{-2}, $V_{oc} = \sim 2.30$ V, FF = ~85.5%, and $P_{max}/A_c = 50.68$ mW cm^{-2} (93.2% power increase against the control device value). Note that minor discrepancies between the calculated and measured values would come from the assumptions during calculation for simplicity (e.g., the normal incidence of waveguided photons, photocurrent generation only at emitter/base). Meanwhile, it is noteworthy that no performance degradation was observed at the module with the scattering waveguide, as it efficiently operates under obliquely incident light (Fig. S8). The temperature coefficient of this module was measured to -0.275% °C^{-1}, reflecting a slight increase in J_{sc} and substantial decreases in V_{oc} and FF (Fig. S9), as expected from the literature[35]. The sudden drop in FF at high temperatures (> 140°C) was most likely due to an increase in series resistance caused by the thermal expansion of via-holes used for metal interconnection.

Photon waveguide properties

To evaluate the photon delivery performance of the experimental PU/glass/$BaSO_4$-PDMS waveguide, series tests were conducted at various f_{BaSO4} values and conditions of the BSR inclusion. Figure 4a provides photographic images of the waveguide samples, depicting light-spreading for centrally incident point sources of blue, green, or red lights. Regardless of the color, light-spreading due to photon scattering rapidly decreased as f_{BaSO4} increased. This implies that the photon scattering contribution of high-f_{BaSO4} waveguides is spatially limited to nearby cells. When comparing the waveguide samples without and with BSR, extended light-spreading was found in the BSR samples under an identical f_{BaSO4} condition. This is because the BSR could create a double path for downward photons, which compensates for the limited light scattering. This behavior can be illustrated in the experiment of the area-confined (0.5 mm width and 15 mm length) AM 1.5 G solar illumination distant from the cell using a black mask (center-to-edge gap between cell and illumination aperture; d_i). As described in Fig. 4b (BSR-less module) and 4c (BSR-added module), the measured J^*_{sc}s of all modules exponentially decayed along d_i and their decay level intensified with raising f_{BaSO4}. This is due to the exponential extinction of propagating photons, especially in dense scattering components. Quantitatively, the decay rate (α) of the BSR-less module

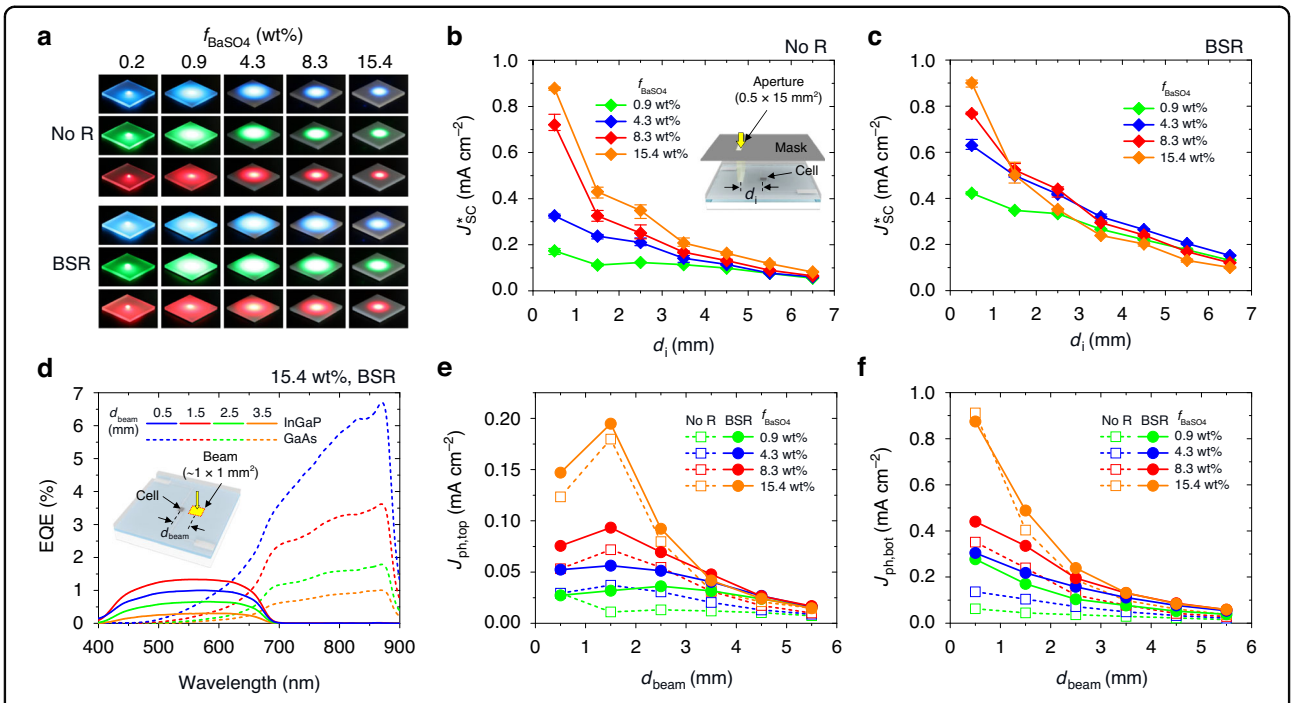

Fig. 4 Photon delivery properties of scattering waveguide module. a Photographic images of the PU/glass/$BaSO_4$-PDMS waveguides without and with BSR under centrally incident blue, green, and red lights at various f_{BaSO4}s. **b, c**, Measured J^*_{sc}s of the BSR-less (**b**) and BSR-added (**c**) modules under the area-confined (0.5 × 15 mm^2 bar) AM 1.5 G solar spectrum as a function of d_i, center-to-edge distance between cell and illumination aperture, at various f_{BaSO4}s. **d**, Measured EQE spectra of the 15.4 wt% BSR-added module at various distances (d_{beam}) between the cell center and beam edge. Estimated $J_{ph,top}$ (**e**) and $J_{ph,bot}$ (**f**) from the EQE spectra for the BSR-less and BSR-added modules as increasing d_{beam} at various f_{BaSO4}s

increased from 0.33 to 0.42 to 0.55 mm^{-1} as f_{BaSO4} changed from 4.3 to 8.3 to 15.4 wt%. On the other hand, the decay rate of the BSR-added module was relatively alleviated at the same f_{BaSO4} conditions (α change from 0.13 to 0.33 to 0.54 mm^{-1}), as expected in the light-spreading configuration test of Fig. 4a. It needs to be mentioned that if only the $BaSO_4$-PDMS scattering sublayer exists without the support of transparent PU/glass sublayers, the photon waveguide deteriorates more rapidly at high f_{BaSO4}, as depicted in Fig. S10.

While the experiments of Fig. 4b, c showed the highest J^*_{sc} at the smallest d_i of 0.5 mm, the scattered photons in immediate proximity to the cell cannot be effectively captured on the front cell surface because enough space is not prepared for redirecting photons by the scattering events behind the cell to the above-cell waveguide. The calculation results for situations of Fig. 4b, c demonstrate this nature, as shown in Fig. S11. Since we believe the accuracy of the narrow bar aperture alignment could not be fully secured in the experiment, we implemented another test to identify the distant illumination effect using a comparative point beam (~1 × 1 mm^2) of the EQE measurement system. Figures 4d and S12 provide measured EQE spectra for the InGaP top cell and the GaAs bottom cell at various distances between the cell and EQE beam (gap between cell center and beam edge; d_{beam}). One obvious fact is that the scattered photons preferentially move to the back surface of the cell as the scattering events occur behind the cell (i.e., top-junction-limited cells). Therefore, designs for higher photon density in the above-cell waveguide channel are essential. The photocurrents of the InGaP ($J_{ph,top}$) and GaAs ($J_{ph,bot}$) cells derived from the measured EQE spectra are summarized in Fig. 4e, f. As mentioned above, the $J_{ph,top}$ exponentially decreased as d_{beam} increased; however, the maximum $J_{ph,top}$ did not appear at the smallest d_{beam} due to insufficient space for guiding the scattered photons to the front cell surface. In contrast, the $J_{ph,bot}$ presents its maximum value at the smallest d_{beam}, which is recognizable because there is no need for circumventive movement of the scattered photons.

Module characterizations at various conditions

To further characterize the scattering waveguide concentrator modules, we implemented several tests, as provided in Fig. 5. Firstly, the effective size of the $BaSO_4$-PDMS scattering sublayer was examined with the setup of (i) spatially confined illumination (square aperture side length; a_i) on the centrally positioned cell and (ii) spatially confined scattering sublayer (square side length; a_{sw}) under the AM 1.5 solar spectrum. Figure 5a, b presents the measured power gain of $P_{max}/P_{max,0}$ (where $P_{max,0}$

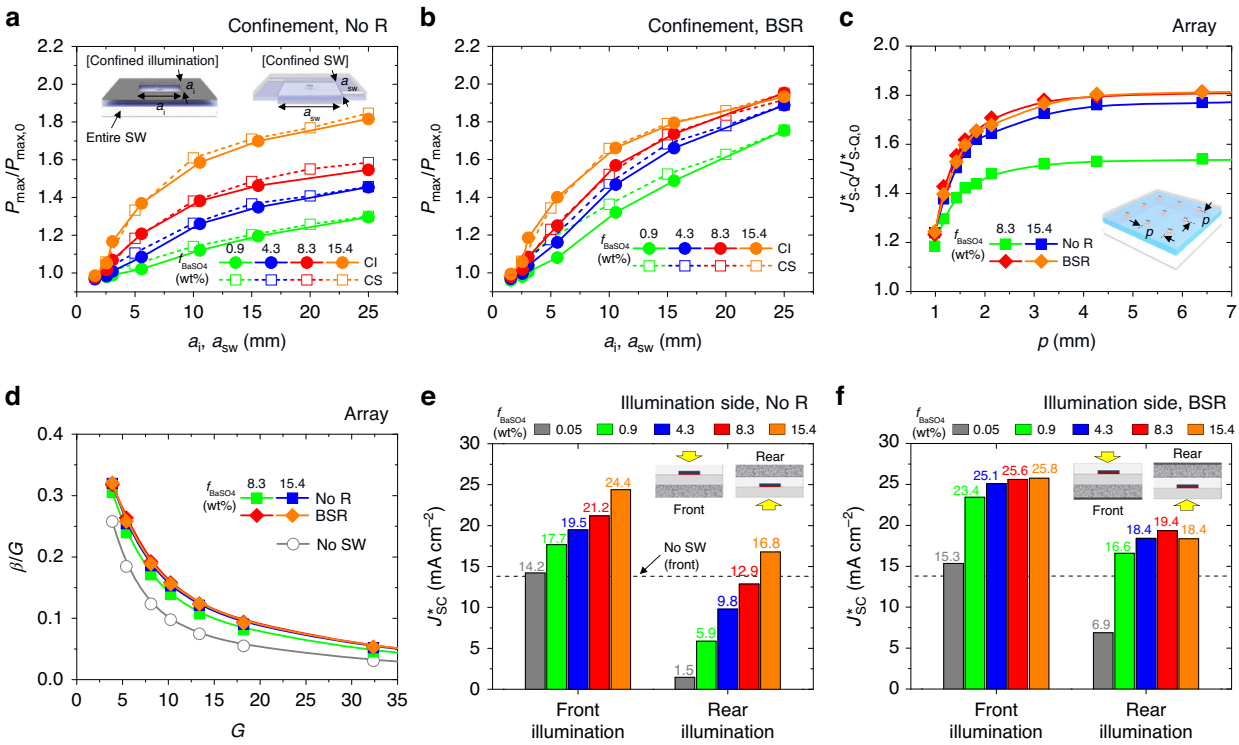

Fig. 5 Module properties at various conditions. Measured power gain $P_{max}/P_{max,0}$ of the BSR-less (**a**) and BSR-added (**b**) modules for spatially square-confined cell illumination (side length: a_i) or $BaSO_4$-PDMS scattering sublayer (side length: a_{sw}) at various f_{BaSO4}s. **c** Calculated current gain $J^*_{S-Q}/J^*_{S-Q,0}$ of the 8.3 and 15.4 wt% arrayed cell modules without and with BSR as a function of cell period p. **d** Derived β/G factors for modules of (**c**) as a function of geometry gain G. β/G of the control module (no SW) also appears for comparison. Measured J^*_{sc}s of the BSR-less (**e**) and BSR-added (**f**) modules when the $BaSO_4$-PDMS scattering sublayer exists on rear (front illumination) or front (rear illumination) surfaces at various f_{BaSO4}s

indicates P_{max} of the control device) as a_i or a_{sw} increased for the BSR-less and BSR-added modules, respectively. While gradually saturating, $P_{max}/P_{max,0}$ of all cases was monotonically raised as a_i or a_{sw} was enlarged. This implies that even though the propagation decay is strict in the scattering waveguide, a larger waveguide can produce a higher $P_{max}/P_{max,0}$ enhancement effect. At similar a_i and a_{sw} values, $P_{max}/P_{max,0}$ with an identical f_{BaSO4} showed analogous levels, indicating that the influence of the scattering sublayer confinement was comparable to that of the light confinement. As expected, a promptly increased $P_{max}/P_{max,0}$ along a_i (or a_{sw}) and its higher maximum were observed in the BSR-added module due to the BSR effect on expanding photon propagation and scattering. The consistent results of this confinement test can be found in the calculation given in Fig. S13.

Secondly, the effective cell period in the waveguide was investigated for modules consisting of a rectangular cell array. Since our calculations deeply correspond to the experiments, this test was conducted only with the calculation for various cell periods (p). Figure 5c provides the current gain of $J^*_{S-Q}/J^*_{S-Q,0}$ (where $J^*_{S-Q,0}$ represents the J^*_{S-Q} of the control device) for the best-performing modules at various p values. While the $J^*_{S-Q}/J^*_{S-Q,0}$ of all modules rapidly increased as p expanded initially, it saturated shortly at $p > \sim 1.8$ mm. It is noteworthy that although a wider illumination may lead to a larger power gain in the confined illumination test, it cannot be understood as forbidding neighboring cells nearby because a certain amount of waveguided photons bypass the neighboring cells. Thus, such a dense array ($p = 1.8 \sim 3.2$ mm) of cells could achieve the full benefit from the scattering waveguide. To more explicitly assess the waveguide module performance, we employed the parameters of the current gain, $\beta = J^*_{S-Q}/J^*_{S-Q,0}$, and the geometry gain, $G = p^2/a_{cell}{}^2$, which derived a factor, $\beta/G = J_{S-Q}/J^*_{S-Q,0}$, a ratio of J_{S-Q} of the arrayed cell module against $J^*_{S-Q,0}$ of the single control cell[6,36]. Assuming the waveguide cost is negligible compared to the cell cost, the G factor indicates the cost reduction ratio and the β/G factor represents the PCE reduction ratio for the arrayed cell module against the single cell[6,37,38]. As illustrated in Fig. 5d, the decrease in β/G level along with the increase in G was considerably mitigated with the scattering waveguide, implying the arrayed cell module can attain the PCE improvement effect by simply incorporating the $BaSO_4$-

PDMS sublayer. For instance, when a relatively large G of 13.4, the β/G factor was improved from 0.075 to 0.124 (65.5% higher) by introducing the scattering waveguide.

Thirdly, we changed the position of the $BaSO_4$-PDMS scattering sublayer from bottom to top and switched the illumination direction accordingly. This test shows the front illumination case is better for obtaining the high J^*_{sc}, as the real illumination case can generate the J^*_{sc} only with the scattered photons behind. Figure 5e, f provides the results of this test for BSR-less and BSR-added modules, respectively. In the case of the BSR-less modules, the J^*_{sc} produced by the rear illumination gradually increased as f_{BaSO4} increased, eventually exceeding $J^*_{sc,0}$ when $f_{BaSO4} = 15.4$ wt% ($J^*_{sc} = 16.8$ mA cm^{-2}) (Fig. 5e). This increase in J^*_{sc} for the rear illumination was over 1.5 times compared to that for the front illumination. When the BSR was added, the scattering and waveguide performance improved, resulting in a further increase in J^*_{sc} up to 19.4 mA cm^{-2}. However, while the real illumination case can lead to a higher net increase of J^*_{sc}, the front illumination case presents a higher absolute J^*_{sc} due to the contribution of direct solar photon incidence.

Discussion

In summary, we proposed a simple strategy to double the output power of multijunction III-V solar cells and systematically studied its principles and properties. We developed a module consisting of microscale InGaP/GaAs transfer-printed coplanarly between PU and glass, with $BaSO_4$ scattering particles-dispersed PDMS attached behind. By regulating the geometrical and optical parameters of the waveguide sublayers to simultaneously collect the flux of directly incident solar photons and waveguided scattered photons at the front surface of the embedded solar cell, we achieved approximately 93% enhancement in output power compared to the module before incorporating the $BaSO_4$-dispersed scattering waveguide. Through a series of additional tests, we examined the effective waveguide size, the validity of arrayed cell module performance enhancement, and the disadvantage of the rear illumination case.

This study demonstrated a straightforward route to improve the power generation of multijunction solar modules comprised of mini-cell arrays. As the multijunction cells should adopt the monofacial configuration, typical BSR or related diffuse BSR cannot operate well without sophisticated but uncomplicated waveguide designs. While the micro-lens technique may offer superior light concentration, the present scattering waveguide technique does not require as strict a sun-tracking system as the micro-lens concentrators due to its focal-free operation. The scattering waveguide could potentially complement the micro-lens concentrator, particularly in scenarios involving off-normal light incidence. We anticipate our design process and characterization results will provide versatile solution options for enhancing multijunction solar cells.

Materials and methods

Fabrication of transfer-printed InGaP/GaAs solar cells

Epitaxial materials of InGaP/GaAs double-junction solar cells were grown on a p-type (001) GaAs wafer using metal-organic chemical vapor deposition (MOCVD, AIX 200/4). The fabrication of transfer-printed double-junction solar microcells started with the electron beam evaporation (Infovion) of n-type ohmic metal contact (AuGe/Ni/Au = 100/30/100 nm), followed by wet chemical etching of n^+-GaAs top contact layer using a mixture of citric acid and hydrogen peroxide ($C_6H_8O_7$:H_2O_2 = 4:1 by volume). Subsequently, the formation of cell mesa (500 × 500 μm^2) structure by photolithography (AZ5214, AZ Electronic Materials) and wet chemical etching in a mixture of 15 ml HBr, 1 g $K_2Cr_2O_7$ and 15 ml deionized (DI) water were conducted. After the thermal deposition of ZnS on the exposed window layer as a single-layer ARC, an additional mesa area (560 × 560 μm^2) was defined to isolate individual cells by wet chemical etching (HBr/ $K_2Cr_2O_7$/DI water) and the exposed AlAs was partially etched by HF. Photoresist (AZ4620, AZ Electronic Materials) was then spin-coated as a polymeric anchor, followed by the formation of etch holes on the second mesa region by photolithography and wet chemical etching (HBr/$K_2Cr_2O_7$/DI). Transferable cells were released from the growth wafer with a PDMS elastomeric stamp (Sylgard 184, Dow Corning) after the selective undercut etching of the AlAs sacrificial layer in diluted HCl solution (HCl:DI water = 3:1 by volume). Released microcells were printed on a glass substrate using photocurable adhesive (~1 μm), and thereafter the remaining p-GaAs base and p-$In_{0.51}Ga_{0.49}P$ back surface field (BSF) layer on the additional mesa were removed in $C_6H_8O_7$/H_2O_2 (4:1 by volume) and H_3PO_4/HCl/DI water (1:1:1 by volume), respectively. On the exposed p-GaAs bottom contact layer, the p-type ohmic metal contact (Cr/Au = 20/100 nm) was then deposited by electron beam evaporation, and electrical passivation except for via-hole of p- and n- contacts was then configured using an insulating layer (SU-8 2002, AZ Electronic Materials). Lastly, the metal bus electrodes (Cr/Au/Cr = 30/1500/30 nm) were deposited for interconnecting metal contacts by thermal evaporation, and transparent PU (NOA61, Norland Products) were drop-casted and subsequently cured to form a top-side waveguide.

Fabrication of attachable scattering waveguide sublayer

To prepare a detachable scattering waveguide sublayer, the weighed BaSO4 (97.5%) powder was mixed with PDMS polymer and curing agent (10:1 by weight). The mixture was degassed and then transferred into glass square molds.

After thermally curing at 65 °C for 120 min, the thickness of the resulting scattering waveguide was 1.9 mm. The scattering waveguide defined in the same size as the glass substrate was attached at the back of the glass substrate. For adding the BSR, a thermally deposited Ag mirror was placed at the rear surface of the scattering waveguide.

Characterization of optical and photovoltaic properties

Diffuse transmission and reflection of scattering waveguides were measured by a homemade optical setup consisting of a white light source, spectrometer (Maya pro 2000, Ocean Optics), and integrating sphere (RTC-060-SF, Labsphere). Current-voltage curves of InGaP/GaAs solar cells were obtained at room temperature using a source meter (Series 2400, Keithley) and a full-spectrum solar simulator with AM 1.5 G spectrum filter (K3000, McScience), where the 1-sun intensity was calibrated using a reference cell (K801S-K070, McScience). EQE measurements of solar cells were conducted by a commercial quantum efficiency measurement system (QuantX 300, Oriel) equipped with a white bias source (IQE-LIGHT-BIAS, Oriel).

Ray-optic simulation

Optical simulations of modules were carried out using commercial ray-tracing software (LightTools, Synopsys). To improve the accuracy (an error rate of ~5%), the number of incident rays of the light source for each wavelength (ranging from 400 to 900 nm) was set to 10^7. Some of the refractive indices of the optical modeling were designed based on the software database, and the others were taken from the literature[38–41]. To simulate the scattering waveguide similar to the experiment, the $BaSO_4$ powder dispersed in PDMS was set to Mie scattering particles with a size of 10–700 nm, and the measured diffuse reflection of scattering waveguides was used to calculate the number density of $BaSO_4$ particles. Details of the simulation setup can be found in Table. S1.

Acknowledgements

This work was supported in part by the research fund of Hanyang University (HY-202300000003126), in part by the National Research Foundation of Korea (NRF) funded by the Ministry of Science, ICT under Grants RS-2023-00209380, RS-2024-00415821, NRF-2021M3H4A6A01048300, NRF-2021M3H4A1A02051253, and NRF-2022M318A2078705, and in part by the Technology Innovation Program (20018379, Development of high-reliability light-emitting fiber-based woven wearable displays) funded by the Ministry of Trade, Industry & Energy of the Republic of Korea.

Author details

[1]School of Electrical Engineering, Korea Advanced Institute of Science and Technology (KAIST), Daejeon 34141, Republic of Korea. [2]Optoelectronic Convergence Research Center, Korea Photonics Technology Institute, Gwangju 61007, Republic of Korea. [3]Department of Applied Physics, Kyung Hee University, Yongin 17104, Republic of Korea. [4]Department of Electrical Engineering, Hanyang University, Seoul 04763, Republic of Korea. [5]Division of Materials Science and Engineering, Hanyang University, Seoul 04763, Republic of Korea

Author contributions

S.-M.L. conceived the idea, led the project, and organized the manuscript contents. S.H.L. developed all photovoltaic devices and performed their characterization with J.-H.K. and S.-K.K. H.J.K. and G.Y.P. implemented the epitaxial growth of solar cells. S.H.L., H.J.K., and S.-M.L. analyzed the experimental data. S.L. and S.-M.L. conducted the optical modeling and interpreted the data from the modeling. S.H.L., H.-J.K., and S.-M.L. discussed and investigated all results. S.H.L. and S.-M.L. wrote the manuscript, and all authors reviewed it and provided feedback.

Conflict of interest

The authors declare no competing interests.

Supplementary information The online version contains supplementary material available at https://doi.org/10.1038/s41377-024-01628-6.

Received: 8 May 2024 Revised: 2 September 2024 Accepted: 5 September 2024
Published online: 20 September 2024

References

1. Geisz, J. F. et al. Six-junction III–V solar cells with 47.1% conversion efficiency under 143 suns concentration. *Nat. Energy* **5**, 326–335 (2020).
2. Vurgaftman, I., Meyer, J. R. & Ram-Mohan, L. R. Band parameters for III–V compound semiconductors and their alloys. *J. Appl. Phys.* **89**, 5815–5875 (2001).
3. Dupré, O., Vaillon, R. & Green, M. A. Physics of the temperature coefficients of solar cells. *Sol. Energy Mater. Sol. Cells* **140**, 92–100 (2015).
4. Hirst, L. C. et al. Intrinsic radiation tolerance of ultra-thin GaAs solar cells. *Appl. Phys. Lett.* **109**, 033908 (2016).
5. Gruginskie, N. et al. Electron radiation–induced degradation of GaAs solar cells with different architectures. *Prog. Photovolt.* **28**, 266–278 (2020).
6. Lee, S. H. et al. Tailoring luminescent solar concentrators for high-performance flexible double-junction III-V photovoltaics. *Adv. Funct. Mater.* **33**, 2210357 (2023).
7. Colter, P., Hagar, B. & Bedair, S. Tunnel junctions for III-V multijunction solar cells review. *Crystals* **8**, 445 (2018).
8. Cotal, H. et al. III-V multijunction solar cells for concentrating photovoltaics. *Energy Environ. Sci.* **2**, 174–192 (2009).
9. Raj, V. et al. Topical review: pathways toward cost-effective single-junction III-V solar cells. *J. Phys. D: Appl. Phys.* **55**, 143002 (2022).
10. Kayes, B. M. et al. Flexible thin-film tandem solar cells with >30% efficiency. *IEEE J. Photovolt.* **4**, 729–733 (2014).
11. Haggren, T., Tan, H. H. & Jagadish, C. III-V thin films for flexible, cost-effective, and emerging applications in optoelectronics and photonics. *Acc. Mater. Res.* **4**, 1046–1056 (2023).
12. Sun, C. et al. Hybrid high-concentration photovoltaic system designed for different weather conditions. *Sci. Rep.* **13**, 5206 (2023).
13. Takamoto, T., Washio, H. & Juso, H. Application of InGaP/GaAs/InGaAs triple junction solar cells to space use and concentrator photovoltaic. Proceedings of the IEEE 40th Photovoltaic Specialist Conference (PVSC). Denver, CO, USA: IEEE, 2014, 1-5.
14. Baba, M. et al. Feasibility study of two-terminal tandem solar cells integrated with smart stack, areal current matching, and low concentration. *Prog. Photovolt.* **25**, 255–263 (2017).
15. Lee, S. M. et al. Synergistically enhanced performance of ultrathin nanostructured silicon solar cells embedded in plasmonically assisted, multispectral luminescent waveguides. *ACS Nano* **11**, 4077–4085 (2017).
16. You, Y. M. et al. Eco-friendly colloidal quantum dot-based luminescent solar concentrators. *Adv. Sci.* **6**, 1801967 (2019).
17. Park, K. et al. Retracted article: luminescent solar concentrator efficiency enhanced via nearly lossless propagation pathways. *Nat. Photonics* **18**, 177–185 (2024).
18. Cho, W. et al. See-through flexible photovoltaic modules of ultrathin silicon solar microcells enhanced by synergistic luminescent and reflective near-infrared backplanes. *Adv. Optical Mater.* **11**, 2300638 (2023).
19. Chou, C. H., Chuang, J. K. & Chen, F. C. High-performance flexible waveguiding photovoltaics. *Sci. Rep.* **3**, 2244 (2013).

20. Zhang, Y. et al. Quantifying mie scattering in luminescent solar concentrators for improved performance. *ACS Photonics* **10**, 3095–3104 (2023).
21. Chou, C. H., Hsu, M. H. & Chen, F. C. Flexible luminescent waveguiding photovoltaics exhibiting strong scattering effects from the dye aggregation. *Nano Energy* **15**, 729–736 (2015).
22. Liu, H. C. et al. Scattering enhanced quantum dots based luminescent solar concentrators by silica microparticles. *Sol. Energy Mater. Sol. Cells* **179**, 380–385 (2018).
23. Lunardi, M. M. et al. Life cycle assessment of tandem LSC-Si devices. *Energy* **181**, 1–10 (2019).
24. Phelan, M. et al. Outdoor performance of a tandem InGaP/Si photovoltaic luminescent solar concentrator. *Sol. Energy Mater. Sol. Cells* **223**, 110945 (2021).
25. Li, J. M. et al. Reliable and high quality adhesive bonding for microfluidic devices. *Micro Nano Lett.* **12**, 90–94 (2017).
26. Zhao, G., Wang, T. M. & Wang, Q. H. Friction and wear behaviors of the polydimethylsiloxane bishydroxyalkyl-terminated modified polyurethane composites filled with the barium sulfate in dry friction and water lubrication. *J. Macromol. Sci., Part B* **50**, 2178–2192 (2011).
27. Lee, S. M. et al. High performance ultrathin GaAs solar cells enabled with heterogeneously integrated dielectric periodic nanostructures. *ACS Nano* **9**, 10356–10365 (2015).
28. Lee, S. M. et al. Printable nanostructured silicon solar cells for high-performance, large-area flexible photovoltaics. *ACS Nano* **8**, 10507–10516 (2014).
29. Cho, S. H. et al. Plasmonically engineered textile polymer solar cells for high-performance, wearable photovoltaics. *ACS Appl. Mater. Interfaces* **11**, 20864–20872 (2019).
30. Shockley, W. & Queisser, H. J. Detailed balance limit of efficiency of p-n junction solar cells. *J. Appl. Phys.* **32**, 510–519 (1961).
31. Miller, O. D., Yablonovitch, E. & Kurtz, S. R. Strong internal and external luminescence as solar cells approach the Shockley-Queisser limit. *IEEE J. Photovolt.* **2**, 303–311 (2012).
32. Guillemoles, J. F. et al. Guide for the perplexed to the Shockley-Queisser model for solar cells. *Nat. Photonics* **13**, 501–505 (2019).
33. De Vos, A. Detailed balance limit of the efficiency of tandem solar cells. *J. Phys. D: Appl. Phys.* **13**, 839–846 (1980).
34. Brown, A. S. & Green, M. A. Detailed balance limit for the series constrained two terminal tandem solar cell. *Phys. E: Low.-dimensional Syst. Nanostruct.* **14**, 96–100 (2002).
35. Singh, P. & Ravindra, N. M. Temperature dependence of solar cell performance-an analysis. *Sol. Energy Mater. Sol. Cells* **101**, 36–45 (2012).
36. Zhao, H. G. et al. Perovskite quantum dots integrated in large-area luminescent solar concentrators. *Nano Energy* **37**, 214–223 (2017).
37. Roncali, J. Luminescent solar collectors: Quo vadis? *Adv. Energy Mater.* **10**, 2001907 (2020).
38. Rafiee, M. et al. An overview of various configurations of luminescent solar concentrators for photovoltaic applications. *Opt. Mater.* **91**, 212–227 (2019).
39. Johnson, P. B. & Christy, R. W. Optical constants of the noble metals. *Phys. Rev. B* **6**, 4370–4379 (1972).
40. Aspnes, D. E. et al. Optical properties of AlxGa1−xAs. *J. Appl. Phys.* **60**, 754–767 (1986).
41. Norland optical adhesive 61. 2021. at https://www.norlandprod.com/adhesives/noa61pg2.html URL.